

Using finite element and Okada models to invert coseismic slip of the 2008 Mw 7.2 Yutian earthquake, China, from InSAR data

Chisheng Wang · Xinjian Shan · Changlin Wang ·
Xiaoli Ding · Guohong Zhang · Timothy Masterlark

Received: 31 August 2011 / Accepted: 16 July 2012
© Springer Science+Business Media B.V. 2012

Abstract We invert InSAR from ascending and descending passes of ENVISAT/ASAR data to estimate the distribution of coseismic slip for the 2008 Mw 7.2 Yutian earthquake by separately using uniform finite element models (FEMs), non-uniform FEMs, and analytical elastic half-space (Okada) models. We use the Steepest Descent method and Laplacian smoothing to regularize and estimate the slip distribution for each of these different models. Fault surface ruptures interpolated from Quickbird optical images constrain the strike of the fault. The

uniform FEM and Okada models assume a fault embedded in a homogeneous and elastic finite domain or half-space, respectively, while the non-uniform FEM describes a domain with spatially variable elastic properties according to the geological structure of Tibet plateau and Tarim. We find that the estimated slip distribution of the non-uniform FEM is similar to that of the uniform FEM but has a slightly larger moment (~2 %). However, more noticeable discrepancies occur between the slip distributions of the uniform FEM and Okada model, where the slip pattern estimated with the FEM looks more scattered and locates at a lower depth. We conclude that, for the case of the Yutian earthquake, the improvement brought by simulating the distribution of geologic material properties is insignificant. This suggests that the uniform geologic structure of Okada models may be sufficient for simulating large intra-continental earthquakes.

C. Wang · X. Shan (✉) · G. Zhang
State Key Laboratory of Earthquake Dynamics,
Institute of Geology, China Earthquake Administration,
Dewai Street, Qijiahuozi, Chaoyang District,
Beijing 100029, China
e-mail: xjshan@163.com

C. Wang · X. Ding
Department of Land Surveying and Geo-Informatics,
The Hong Kong Polytechnic University,
Hong Kong, China

C. Wang
Center for Earth Observation and Digital Earth,
Chinese Academy of Science,
Kedian Tower F14, No. 9 Beiyitiao Road, Zhongguancun,
Haidian District,
Beijing 100190, China

T. Masterlark
Department of Geology and Geological Engineering,
South Dakota School of Mines and Technology,
Rapid City, SD 57701, USA

Keywords Finite element model · Okada model ·
Yutian earthquake · Coseismic slip · InSAR

1 Introduction

With advanced geodetic technologies like GPS and InSAR, the static surface displacements of almost all large onshore earthquakes occurring in the past decade have been studied in detail (e.g., Wright et al. 2003; Schmidt and Burgmann 2006; Chlie et al. 2007; Shen et al. 2009; Hayes et al. 2010; Guerrieri et al. 2010;

Zhang et al. 2011; Wang et al. 2012). By inverting these abundant deformation measurements, with an appropriate deformation model, it is possible to estimate the distribution of coseismic slip along a fault. Deformation models simulate deformation caused by elastic dislocation (slip) along a fault embedded in the Earth's internal structure and thus provide the linkage between surface deformation and the fault slip at depth. Deformation models of slip can be grouped into two broad categories: Okada-type models, represented by analytical solutions (e.g., Okada 1992, 1985), and numerical models, represented by finite element models (FEMs) (e.g., Masterlark 2003; Masterlark et al. 2001; Wang et al. 2009).

Okada models assume an elastic dislocation embedded in a homogeneous elastic half-space (HEHS). Because of their computational efficiency, Okada models are commonly applied to analyses of coseismic deformation observed with geodetic data. Alternatively, FEMs can simulate a dislocation embedded in an elastic problem domain of arbitrary geometric complexity, comprising a distribution of material properties. Only a limited number of studies have investigated the FEM application in coseismic slip inversion. In order to make a better choice between the FEM and traditional Okada model in coseismic deformation modeling, it is necessary to explore the capabilities of FEMs and understand their differences from analytical methods.

Methods for embedding elastic dislocations in FEMs to simulate slip along a fault was introduced by Smith (1974), using the method of kinematic constraint equations. Melosh and Raefsky (1981) later introduced the split node method to simulate elastic dislocations for FEMs. While researches regularly use FEM for preseismic (e.g., Fialko 2006) or postseismic modeling (e.g., Hu et al. 2004), the application of FEMs in inverse analyses for coseismic deformation is rare. Among the limited number of FEM coseismic modeling studies, Currenti et al. (2008) described the general procedure for FEM inversion with quadric programming algorithm; Masterlark (2003) analyzed the sensitivities to HEHS assumption by comparing the inverted slip difference from uniform FEM and non-uniform FEM; Hearn and Burgmann (2005) discussed the effects of elastic layering in a strike-slip earthquake by using FEM, Okada, and semi-analytical models; Zhao et al. (2004) used some forward FEM and Okada models to test the surface displacement

changes brought from crustal rigidity layering and lateral variations. FEM-based InSAR analyses, such as this study, are beginning to emerge for the case of coseismic slip along normal faults (e.g., Trasatti et al. 2011).

In order to obtain better understanding of FEM coseismic slip inversion, particularly for a continental normal-faulting earthquake constrained by InSAR, this paper takes the 2008 Mw 7.2 Yutian earthquake (YE) as an example to implement coseismic slip inversion by using FEMs and Okada models separately. The Okada models simulate the HEHS assumptions while FEMs simulate both HEHS and non-HEHS configurations. InSAR observations from the Envisat satellite with two observing directions are applied for geodetic constraints. In the end, we present detailed slip inversions for the 2008 Mw 7.2 Yutian earthquake by using these three model configurations with various parameters, make comparisons, and discuss the differences between them.

2 Method

With a priori geometry and configuration of elastic material properties, the relationship between fault slip (elastic dislocation) and crustal deformation follows a linear formula:

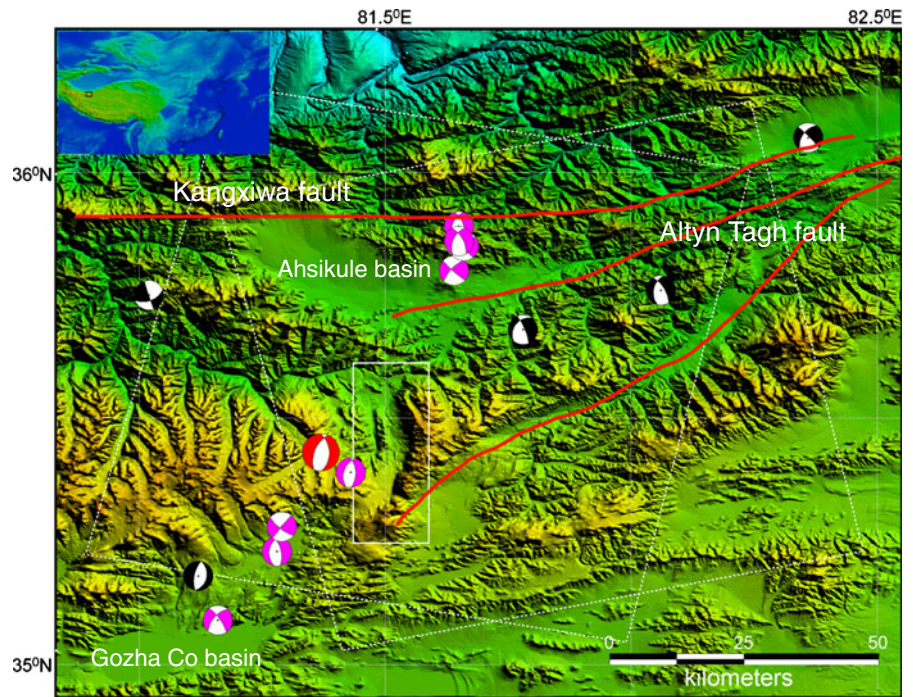
$$d_i = \sum_j G_{ij}s_j \quad (1)$$

where d_i is the displacement of the i th observation point and s_j is the dislocation of the j th fault patch. Each G_{ij} is a displacement component at location i due to a unit dislocation of fault patch j . The computation of the matrix of Greens functions, \mathbf{G} , for N observation points and M fault patches requires $M \times 2$ (strike-slip and dip-slip components) forward model runs for the displacement vector (d) of length N . We neglect the tensile (opening) component, which is not supported by the focal mechanism (Fig. 1).

The inverse problem of predicted deformation due to a given slip event is to find the unknown slip value of each fault patch that enables a minimum misfit (ϕ_d) and a smoothing function (ϕ_r):

$$\phi = \phi_d + \lambda\phi_r = \frac{1}{2} \left[(\mathbf{d}_{\text{pre}} - \mathbf{d}_{\text{obs}})^T (\mathbf{d}_{\text{pre}} - \mathbf{d}_{\text{obs}}) \right] + \lambda^2 \phi_r \quad (2)$$

Fig.1 Shaded topographic relief map showing the tectonic setting of Yutian earthquake. *Red lines* indicate regional faults. The areas covered by ASAR in ascending and descending track are shown as *white dashed rectangles*. The *white solid box* is the area covered by Quickbird image. The *pink focal mechanism solutions* denote Yutian aftershocks. The *black focal mechanism solutions* are $M_s \geq 5$ shocks from 1 January 1976 to 20 March 2008. The *red focal mechanism solution* is M_w 7.2 mainshock (all focal mechanism solutions are from Global GMT). Background is 3 s DEM from <http://www2.jpl.nasa.gov>



where \mathbf{d}_{obs} and \mathbf{d}_{pre} are the observed and predicted displacement vectors, respectively, and λ is the smoothing factor that controls the tradeoff between a solution that minimizes misfit or roughness. The smoothing function is:

$$\phi_r = \mathbf{s}^T \mathbf{L}^T \mathbf{L} \mathbf{s} \quad (3)$$

where \mathbf{s} is the vector of slip patch dislocations and \mathbf{L} is a Laplacian operator implemented with a finite difference formulation (Masterlark 2003). This study used a Fortran code called SDM, provided by Dr. Wang Rongjiang in GeoForschungsZentrum Potsdam, to implement the inversion process. SDM code is a slip inversion code which adopts the Steepest Descent method to solve for the slip distribution on fault plane from surface deformation data, which is the inverse problem as described in Eq. (2). In this study, two approaches are employed to generate \mathbf{G} .

2.1 Okada approach

The first approach used to generate Greens functions uses analytical solutions. The Okada model (Okada 1985, 1992) is commonly used in inversions of geodetic data to estimate fault slip. The Okada model predicts surface displacement according to a specified rectangular dislocation at depth. The SDM code has

included the Okada's subroutine DC3D. The Okada model assumes a homogeneous elastic half-space. We initialize both Lamé parameters to be 4×10^{10} Pa, which is equivalent to a Young's modulus of 100 GPa and Poisson's ratio of 0.25.

2.2 FEM approach

We use the finite element code Abaqus (www.simulia.com) for constructing FEMs in this study. The code solves for displacement (u) for a problem domain having elastic properties and specified configuration of boundary and initial conditions. Expressed in index notation, the three governing equations for elastic materials are:

$$G \nabla^2 u_i + \frac{G}{(1-2\nu)} \frac{\partial^2 u_k}{\partial x_i \partial x_k} = -F_i \quad (4)$$

where G is the shear modulus, ν is Poisson's ratio, and F is a body force per unit volume (Wang 2000). The subscript i spans orthogonal direction components 1, 2, and 3 and the subscript k implies summation over these three components. Abaqus-based FEMs were used in inverse analyses of GPS-observed crustal deformation for the 2011 M9 Tohoku earthquake (Grilli et al. 2012), 2004 M9 Sumatra–Andaman earthquake (Masterlark and Hughes 2008), and the 1995 M8

Jalisco–Colima earthquake (Masterlark 2003) in an effort to address complicated geometries and variations in material properties that cannot be addressed in standard elastic half-space models (Okada 1992).

In this work, we construct two FEMs for the Yutian earthquake, one with the assumption of a homogeneous domain and another complying with the geologic situation, where the model domain has layered and lateral variations. The first model is for comparison with the Okada model, which shares the homogeneous assumption. Prediction differences between these models are attributed to differences in domain geometry, boundary conditions, and numerical artifacts of the FEM mesh. Predictions from non-uniform FEM are compared to those of the uniform FEM with the purpose of demonstrating how the layered and lateral variations affect the estimated slip distribution.

3 Yutian earthquake: data and model configuration

On 21 March 2008, the Mw 7.2 YE struck the boundary between Yutian and Qira counties, Xinjiang, at the northern margin of the Kunlun Mountains in western China (Fig. 1). The tectonic features of Tibet are dominated by large low-angle thrusting faults of the Himalayan front in the south and several large strike-slip faults along the edges or in the interior of the plateau. Studies show that the India plate continues to move northward at 50 mm/year after the India–Eurasia collision (Shen et al. 2001). Rupture of the YE occurred on the southwest segment of Altyn Tagh strike-slip belt, which is a tectonic boundary between the Tibetan plateau and Tarim basin in the northwest (Molnar et al. 1987). This fault segment accommodates the sinistral motion between the Tibetan plateau and the Tarim block within the India–Eurasia collision zone. Geodetic data suggest that the fault slip rate is about 10 mm/year (Wallace et al. 2004; Zhang et al. 2007).

3.1 Satellite data

Two Quickbird colored fusion satellite images (0.61 m in resolution) of the region were taken to map the fault trend of Yutian earthquake. They were separately acquired at 30 July 2008 and 11 May 2008. Through rupture features on the surface recognized from

Quickbird images, such as fissures, scarps, collapses, and fault-bounded blocks, we can accurately map the fault trace in this event with the assumption that fault slip breaks from the depth up to the surface (Fig. 2a). Interested readers may refer to Shan et al. (2010) for a detailed interpretation of Quickbird images. In order to simplify the overall complex fault trace pattern, we fit the fault trace with three straight line segments (Table 1). The dip angle of fault planes conforms to parameters given by Harvard CMT focal mechanism solution.

The SAR interferograms were generated by C-band ENVISAT/ASAR data from two tracks (both descending and ascending passes) with the 2×4 multilooking operator (Fig. 2b). The descending pass image pair passed from 01 April 2007 to 20 April 2008, while the ascending pass image pair was from 22 February 2008 to 02 May 2008 (Wang et al. 2009). We used a two-pass technique to process the data with the GAMMA software (Wegmuller and Werner 1997). The topography component was removed from the interferograms by using the 3-s SRTM DEM that has a vertical accuracy of about 16 m. The minimum flow cost algorithm was used to unwrap the masked interferograms where coherence threshold was set as 0.5. Inversion of InSAR deformation at full resolution is computationally expensive (more than 25 million pixels for each image) and we used quadtree techniques to reduce the number of data without losing information (e.g., Masterlark and Lu 2004). Each image is padded into a square array having 2^n pixels per side, where n is a positive integer. The image is divided into quadrants and subquadrants until the largest difference of data in a given quadrant is less than or equal to a specified criterion of 50 mm near the deformation resolution limit of ENVISAT data (Jonsson et al. 2002). To avoid our sampled points from clustering around the boundary, we filled some incoherent areas by the value interpolated from their surrounding points. Finally, 2,606 InSAR points were picked for inversion constraints. The points from two interferogram pairs are weighted equally during the inversion.

3.2 Model configuration

3.2.1 Uniform and non-uniform FEMs

The Yutian earthquake occurred at the boundary between Tibetan plateau and Tarim basin, two blocks composed by a different geophysical structure. We

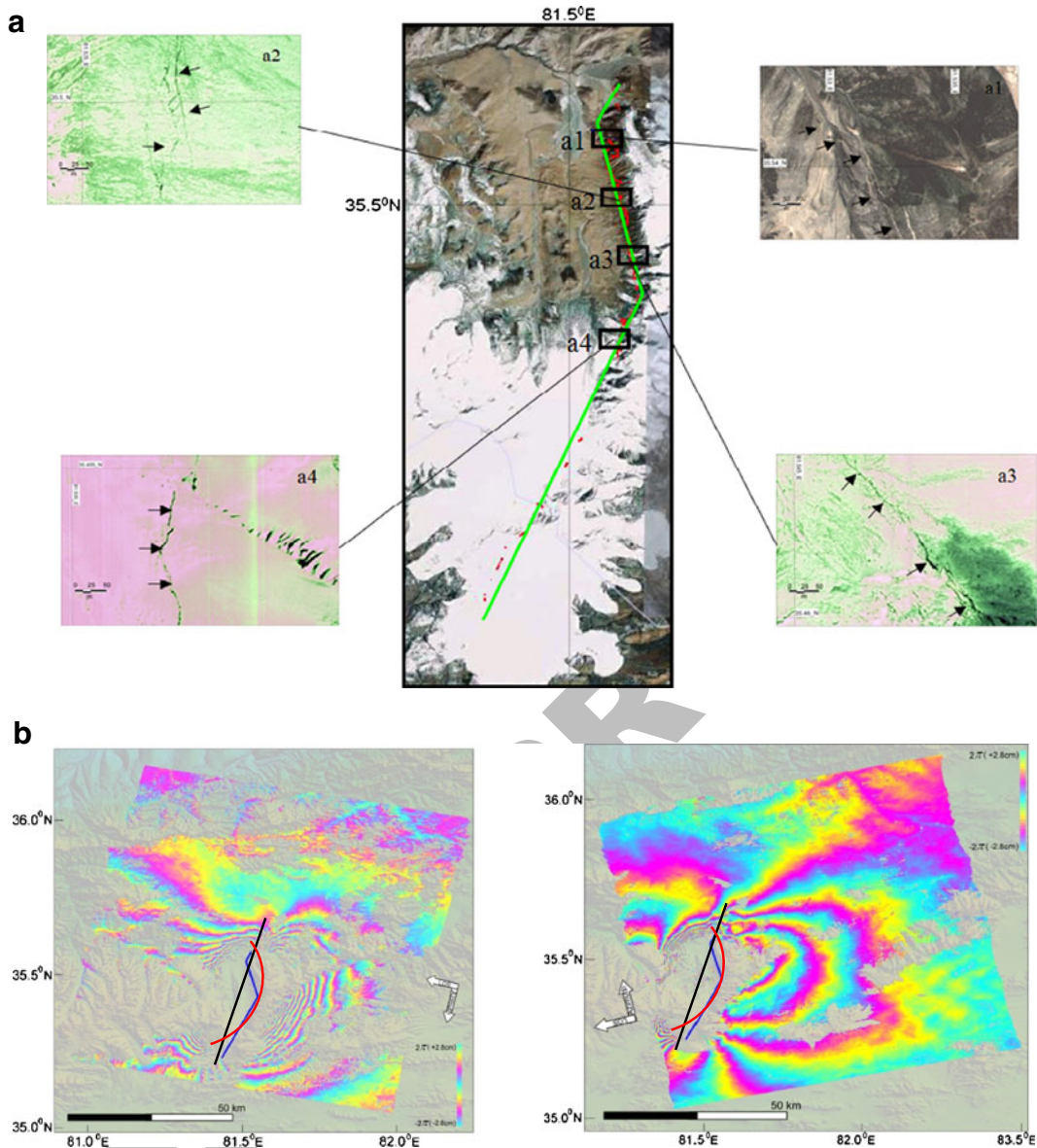


Fig. 2 Quickbird image interpolation (Shan et al. 2010) and InSAR observation of Yutian earthquake. **a** Quickbird images. The *central figure* is the global image of the surface rupture zone produced by the Yutian Ms 7.3 shock from satellite image with Google Earth satellite image as background. Small *black solid boxes* labeled *a1–a4* are focused interpretation portions. The *red solid line* is the interpreted surface rupture zone. The *green solid line* is the simplified fault trace with three linear segments. The surrounding figures are Quickbird images corresponding to

four focused portions in the left figure. **b** InSAR interferogram with decorrelated regions masked. Each “fringe” represents 2.8 cm of range change in LOS. The *blue line* is the surface trace of the fault, inferred from Quickbird images. The *red line* and the *black line* are arc-shaped and one-segment rupture, respectively, which would be used below. Their rupture geometry is summarized in Table 1. The *left image* is the descending-pass interferogram and the *right image* is the ascending-pass interferogram

construct our FEMs based on the geologic survey of conjunction structure (Qiusheng et al. 2002) and on earth layer studies in Tarim (China Seismological Bureau 1992) and Tibet plateau (Shao and Xu

1997). Our model is then divided into three layers in vertical (upper crust, lower crust, and mantle), the interface of which are separately Conrad and Moho discontinuity. In the horizontal cross-section,

Table 1 Rupture geometry

	Three segments			One segment	Arc-shaped
	Segment 1	Segment 2	Segment 3		
North location (longitude, latitude)	(81.55°, 35.60°)	(81.52°, 35.55°)	(81.56°, 35.44°)	(81.57°, 35.64°)	(81.55°, 35.58°)
South location (longitude, latitude)	(81.52°, 35.55°)	(81.56°, 35.44°)	(81.44°, 35.24°)	(81.43°, 35.20°)	(81.38°, 35.25°)
Strike	201°	168°	208°	194°	174°–231°
Dip	54°	53°	55°	52°	52°
Length (km)	6	12.6	25	50	42
Width (km)	30	30	30	20	30
Slip patches, along strike	3	7	12	26	17
Slip patches, down dip	16	16	16	11	16
Patch size, along strike (km)	1.7	1.8	2.1	1.9	2.4
Patch size, down dip (km)	1.9	1.9	1.9	1.8	1.9

we partition the model to simulate the Tarim basin and Tibet plateau. The thicknesses of the three layers in the Tarim basin are 9, 36, and 55 km. For the Tibet plateau, they are separately 30, 30, and 40 km. The rocks of the upper crust, lower crust, and upper mantle are separately dominated by granite, whinstone, and peridotite. For the non-uniform FEM, based on the material property of various rocks (Christensen 1996), we assign three layers with Young modulus as 50, 100, and 150 GPa and Poisson's ratio as 0.23, 0.29, and 0.26. For the uniform FEM, all model materials were assigned with the same elasticity where Young modulus is 100 GPa and Poisson's ratio is 0.25.

The 3D problem domain of the FEM for the Yutian earthquake simulates a 240×240 km-sized large area having a depth of 100 km (Fig. 3a). The FEM consists of two parts, separated by a planar

boundary that includes the fault of the Yutian earthquake. One part represents the hanging wall side of the boundary and the other part represents the footwall side of the boundary. The footwall and hanging wall are welded together (all degrees of freedom are shared by both parts) along this planar surface except for the simulated fault region. The interactions of the two parts along the fault are governed by kinematic constraint equations for node pairs that populate the fault surface (Masterlark 2003; Masterlark and Hughes 2008). The FEM mesh is more refined near the fault, where we expect greater deformation gradients, and gradually coarsens toward the boundaries of the problem domain. The problem domain tessellation includes 87,400 elements and 96,096 nodes. The fault is considered as a rectangular plane of 44×30 km, with its upper boundary intersecting

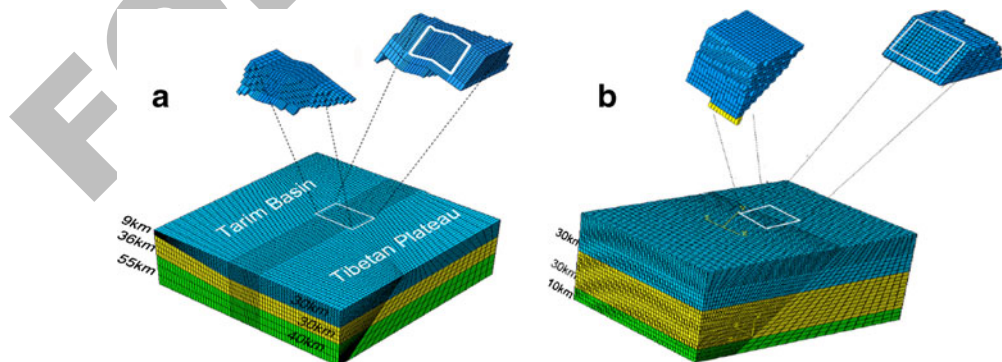


Fig. 3 FEM configuration of Yutian earthquake fault. A local region including the fault plane was extracted in the upper part. **a** Three-segment FEM, **b** one-segment FEM

the land surface. It dips northwest with an angle of $\sim 52^\circ$. The spatial resolution of the fault plane is about 2×2 km. The fault trace conforms to surface rupture identified from Quickbird images (Shan et al. 2010), which include three linear segments (Table 1). For boundary conditions, the base and lateral boundaries are specified as zero displacement, while the top (land) surface is stress-free. Initial conditions are equilibrium. In addition, we construct a one-segment FEM for comparison with one-segment Okada model. It has a 100×100 -km-sized large area with a depth of 70 km, tessellated into 76,908 nodes and 69,972 elements. The fault geometry conforms to one-segment fault parameters given in Table 1.

3.2.2 Okada model

We also define the same fault geometry in the Okada model according to Table 1. The Okada model uses rectangles to describe fault plane, which include overlapping or discontinuous fault segments if the entire fault has variable strike and dip (Sun et al. 2007). Though the fault trace and dip angle of Okada fault generally conforms to the FEM configuration, the fault location and plane sizes differ to some degree. The visualization of FEM and Okada fault geometry difference can be seen in Fig. 6a, where breaks between fault segments exist in the Okada case (left one). The material assignment for the Okada model is the same as uniform FEM, which also has a Young modulus of 100 GPa and Poisson's ratio of 0.25. There is no shallow erosional/weathering layer considered in all our models (both FEM and Okada). During all the below inversions using FEM or Okada models, the rake angle was set in a range from -94° to -54° ($\pm 20^\circ$ around the rake value given by Harvard CMT solution).

4 Results and discussion

4.1 Parameters test

Because both the focal mechanism and the geodetic data may have errors, there would be some uncertainties in fault strike and dip which derived from Harvard CMT solution and QuickBird images. We varied these two parameters in the Okada models to test the sensitivities of inversion results to these parameters. In order to avoid the influence from other factors (e.g., smoothing constraint, rake boundary and grid size), all unrelated parameters are set the same in the test. Please note that the grid size of all models in the test is 2.4×1.9 km, differing from the grid sizes given in Table 1 for some geometries. First, we compared the inversion results from fault models by using three-segment, one-segment, and arc-shape fault geometries. Then, in the three-segment fault geometry, we separately varied the strike angle and dip angle of each segment and compared their corresponding residuals. The strike value are tested in a range of 80° ($\pm 40^\circ$ around the fixed value of Table 1) and the dip angle are tried in a collection varying from 10° to 90° .

The inverted slip distributions by using three fault geometries are shown in Fig. 4. All of them suggest that the fault breaks the surface, having a peak value of around 4 m. There are some significant differences in the slip patterns of three geometries. One-segment geometry gives the simplest slip, which has a semicircle pattern in the center of the fault plane, while arc-shaped geometry has a slip discrepancy along the strike, where north slip is stronger than the south slip. Three-segment geometry distinguishes the slip area into two concentrations: the larger one is located in the north and the weaker one in the south. The misfit between prediction and observation shows that the three-segment geometry fit the InSAR data best

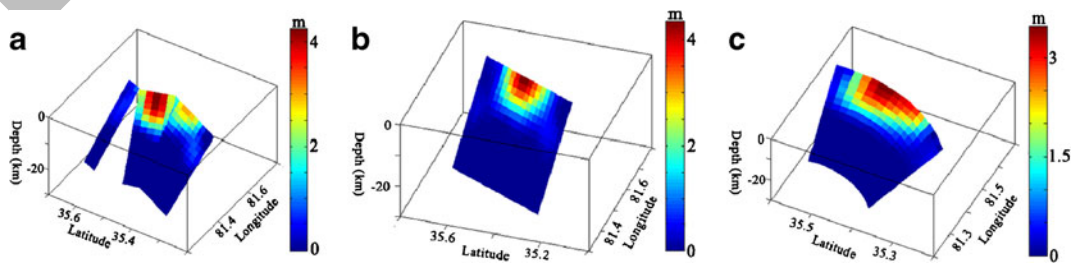


Fig. 4 Slip distribution from three fault geometries. **a** Three segments, **b** one segment, **c** arc-shaped

Table 2 Inversion results by using Okada model with different fault geometries

	RMSE descending dataset (m)	RMSE ascending dataset (m)	Maximum slip (m)	Smoothing factor	RMSE (m)
Arc	0.04	0.035	3.49	0.05	0.037654
One segment	0.041	0.028	4.37	0.05	0.035288
Three segments	0.039	0.029	4.26	0.05	0.034506

(Table 2), having a root mean square error (RMSE) of 3.45 cm.

As shown by the Quickbird high-resolution optical images (Fig. 2a), a great amount of seismic collapses and fault blocks were found in the north of the fracture zone, while in the south the collapses are relatively less, where only some small dribs and drabs were distributed. The simple semicircle slip pattern derived from one-segment geometry has no difference of slip intensity between the north and south part and therefore may not well represent the real slip characteristics. Arc-shaped geometry could derive the slip difference between the south part and the north part; however, its residual is higher than the other two geometries, and the linearly varying strike cannot fit the actual rupture as well as the three-segment geometry. Thus, the three-segment geometry could be considered to represent the real fault the best because it not only illustrates the slip intensity difference between north part and south part but also gives the least RMSE.

Figure 5 shows the variation of root mean square residual by regularly changing each segment's dip and strike parameters in the three-segment geometry. The results show that the RMSE is not sensitive to the

strike and dip change of segment 1, while it fluctuates a lot when the geometry parameters of segment 2 and segment 3 deviate from the fixed value in Table 1. As shown in the three-segment inversion result (Fig. 4a), there is almost no slip found in segment 1. Therefore, the change of segment 1's parameters will not affect the result significantly. However, segment 2 and segment 3 contain most slip features and consequently have large influence on the RMSE. In general, by using the strike and dip parameters in Table 1, we can obtain a satisfactory fit to the observation with an RMSE value of 3.45 cm, which is almost the lowest one among the parameter tests.

4.2 Okada and uniform FEM

To find the inherent difference between FEM and Okada models for the YE, we compared the inversion results from the Okada model and the uniform FEM. The comparisons are implemented in both three-segment and one-segment fault geometries. Firstly, the smoothing factors in both FEM and Okada model are fixed similarly. The value is determined from the trade-off analysis between misfit and roughness of Okada inversion. Then, we estimated another

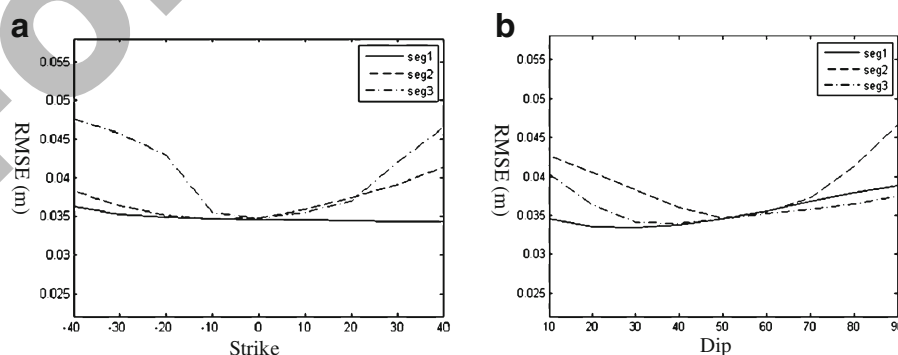


Fig. 5 Parameter test on each segment of a three-segment-geometry Okada model. **a** Strike test; the x -coordinate indicates the degree deviation from a fixed value in Table 1. **b** Dip test

smoothing factor from the trade-off analysis of FEM inversion. The first step could illustrate the difference between FEM and Okada in using the same smoothing factor. The second step could compare their difference in using a self-determined smoothing factor.

Trade-off analysis method is commonly used for determining the smoothing factor of slip inversion (e.g., Wright et al. 2004). The trade-off curves of the Okada inversion indicate a preferred smoothing factor of 0.05 for both three-segment and one-segment fault

geometries. By using the same smoothing factor of 0.05, the corresponding inversion results in FEM and Okada are shown in Fig. 6. For the three-segment geometry, both models result in a slip pattern with two concentrations. The fault dislocation peaks at the north concentration, with a value of 4.4 m in Okada and 6.5 m in FEM. The slip is dominated by a normal faulting mechanism in segment 2 and includes some left-lateral slip in segment 3. The slip area derived from FEM model is less than that from the Okada

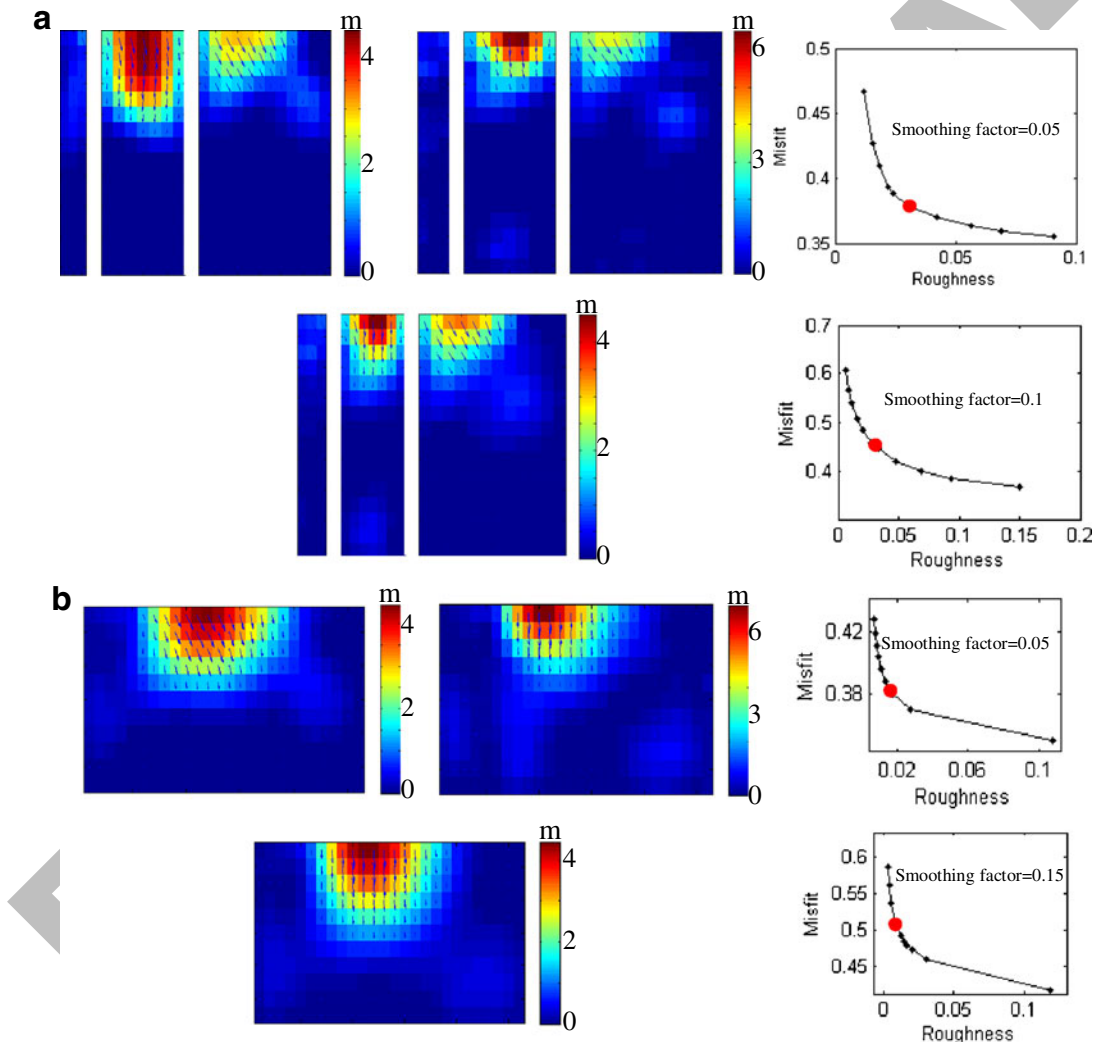


Fig. 6 A series of inversion results, as well as the corresponding trade-off curves, by using different models and different geometries in homogenous half-space. **a** Three-segment geometry. **b** One-segment geometry. For both **a** and **b**, the slip distributions in the first row are inversion results by using the Okada model (*left*) and uniform FEM (*middle*) with a unified smoothing factor. The

corresponding trade-off curve, generated from Okada inversion, is shown at the *right*. The slip distribution in the second row is the inversion result from uniform FEM inversion with self-determined smoothing factor. The *right figure* is the corresponding trade-off curve generated from FEM inversion. The *red points* in trade-off curves are corresponding to the selected smoothing factors

model. We used the following formula to calculate the seismic moment, M_0 :

$$M_0 = \mu \sum_j A_j s_j$$

where μ is the shear modulus, A_j is the rupture area of slip patch j , and s_j is the estimated slip of slip patch j . Assuming a shear modulus of 3×10^{10} Pa, the Okada model suggests a seismic moment of 2.34×10^{19} Nm and the FEM seismic moment is 2.53×10^{19} Nm. The RMSE of the Okada model, 3.45 cm, is less than that of the uniform FEM (Table 3). For the one-segment geometry configuration, the differences between FEM and Okada models are similar to the situation in the three-segment configuration, where the FEM inversion has a greater maximum slip, higher seismic moment, larger RMSE, and a smaller slip area.

Through analyzing the FEM's trade-off curve, we can obtain higher smoothing factors, which are 0.1 and 0.15, respectively, for three-segment and one-segment geometries. The inversion results derived by applying the newly determined smoothing factor are shown in Fig. 6. For the three-segment geometry, the peak slip has dropped to 4.5 m, and the seismic moment has decreased as well to a value of 2.30×10^{19} Nm. The slip area has expanded and the RMSE has increased to 4.2 cm (Table 3). Comparing with previous FEM results, most characteristics of the new FEM are closer to those of Okada, except the difference in RMSE. The one-segment geometry has similar differences after using the self-determined smoothing factor, where maximum slip and seismic moment have dropped, RMSE has increased, and the slip area has expanded.

From the comparison of FEM and Okada in both one-segment and three-segment geometries, it can be found that FEMs generate a more scattered (rougher) slip when the smoothing factor is fixed similarly as

that of Okada. If we would use a self-determined smoothing factor for the FEM, the fit result could get closer to that of Okada, but with the cost of increased RMSE. As FEM and Okada inversions are carried in the same inversion scheme with the same parameter settings, these differences can be attributed to inherent discrepancies between numerical and analytical methods.

We used a forward model to illustrate the inherent differences between an FEM and Okada model for simulating the YE. Figure 7a, b are the displacement fields derived by using an FEM and an Okada model, generated by the one-segment fault geometry with 1 m of uniform dip-slip on the fault plane. The deformation patterns are generally similar, but the FEM is coarser than Okada (e.g., the oscillatory signal in the right part of Fig. 7a). For simulating the HEHS assumptions, the analytical solution is clearly more accurate than the numerical one. The FEM approximates the partial differential equation (Eq. 4) using linear interpolation basis functions. The accuracy of this approximation improves with decreasing nodal spacing, and it is particularly important to minimize the nodal spacing of elements where displacement gradients are greatest. That is, the oscillatory predictions of the FEM (Fig. 7a) are likely caused by the insufficient refinement of the FEM mesh near the fault. Such numerical artifacts will propagate into the inverse method and explain our finding that FEM generated a more scattered slip and required a higher smoothing factor.

Theoretically, an FEM can be designed to closely approximate an Okada model (Masterlark and Hughes 2008). Some forward model tests give approximative coseismic displacement as Okada by using FEMs (Zhao et al. 2004). However, prediction differences between Okada models and FEMs can be substantial, particularly

Table 3 Inversion results by using Okada model and uniform FEM with three- and one-segment fault

	RMSE descending dataset (m)	RMSE ascending dataset (m)	Maximum slip (m)	Smoothing factor	RMSE (m)	Moment (Nm)	Magnitude
OKADA, three segments	0.039	0.029	4.4092	0.05	0.0345	2.34×10^{19}	6.9126
FEM, three segments, same smooth	0.0405	0.0362	6.5	0.05	0.0385	2.53×10^{19}	6.9354
FEM, three segments, self smooth	0.0435	0.0403	4.5163	0.1	0.042	2.30×10^{19}	6.9079
OKADA, one segment	0.041	0.028	4.46	0.05	0.0353	2.25×10^{19}	6.9013
FEM, one segment, same smooth	0.0414	0.0429	7.08	0.05	0.0421	2.73×10^{19}	6.9579
FEM, one segment, self smooth	0.0427	0.0476	4.45	0.15	0.0452	2.41×10^{19}	6.9215

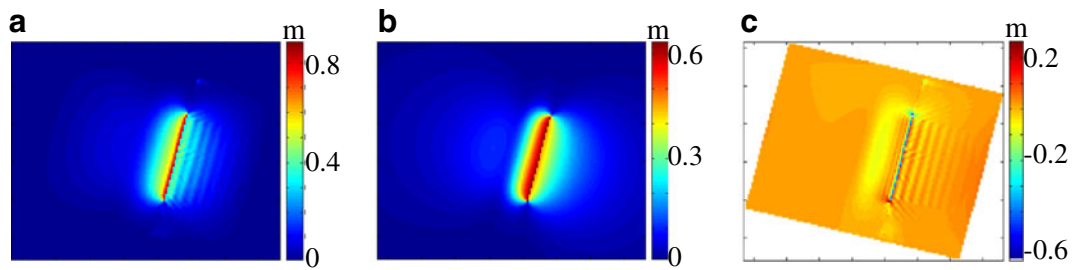


Fig. 7 Forward test by assuming 1-m uniform dip-slip on one-segment geometry. **a** Ground displacement magnitude generated from FEM, **b** ground displacement magnitude generated from Okada, **c** difference between two displacements

for complex 3D geometric configurations when one attempts to coarsen the mesh of an FEM in order to reduce the computation time of calculating Greens functions. In this study, to compute the Greens functions of three-segment FEM, we run 352×3 forward models which are initialized with a unit slip on each fault patch. Each forward model takes 15 min and the whole computation time is almost 10 days. However, the Okada model requires less than 1 min to compute the entire matrix of Greens functions. Given that FEM has lower accuracy and heavy computational burden, it is not necessary to use FEM for coseismic slip inversion if the geologic construction is not too different from HEHS assumptions.

4.3 Non-uniform FEM and uniform FEM

Figure 8 gives slip distributions for the YE by using non-uniform FEMs with three-segment and one-segment fault geometries. In order to avoid the influence of shear modulus in the comparison, we used a unified shear modulus (3×10^{10} Nm) to calculate the seismic moment of the two FEMs. Slight differences are found between fault slip distributions estimated for uniform and layered FEMs. For the three-segment fault geometry, layered and uniform FEMs give seismic moments of 2.35×10^{19} and 2.30×10^{19} Nm, respectively, which are equal to an event of Mw 6.91 or

Mw 6.90. The RMSE for uniform and layered FEMs are the same, with a value of 4.2 cm. For the one-segment fault geometry, the seismic moments of layered and uniform FEMs are 2.47×10^{19} and 2.41×10^{19} Nm, respectively. Similar to the models with three segments, the layered FEM with one segment has a higher moment than the uniform FEM with one segment. The RMSEs given by uniform and layered FEMs are slightly different at 4.52 and 4.48 cm, respectively (Table 4).

It is verified by many scholars that differences brought by breaking the HEHS assumption in the inversion model are larger than the uncertainty of geodetic measurement (Masterlark 2003; Zhao et al. 2004). The consideration of layered elastic structure is possible to generate a larger seismic potency and centroid depth for shallow earthquakes (Savage 1987; Savage 1998; Pollitz 1996; Rybicki 1971; Hearn and Burgmann 2005). Like these previous studies, our non-uniform model also gives a larger moment than the uniform model. However, this difference only accounts for $\sim 2\%$ of the inverted moment. Although our geological satisfying model has considered both lateral variation and layered construction according to the geologic setting in Tarim basin, the difference of slip pattern between uniform and non-uniform is insignificant.

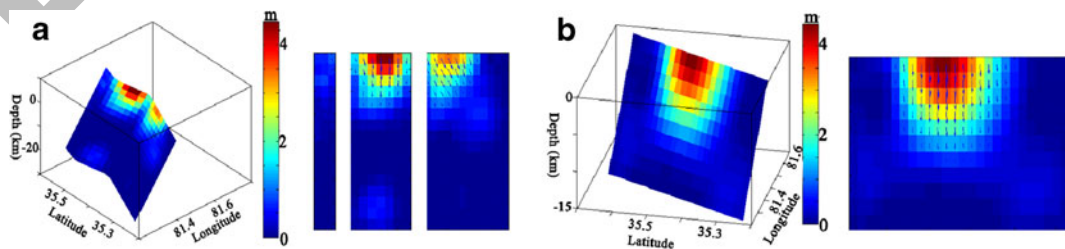


Fig. 8 Slip distribution inverted from non-uniform FEM. **a** Using three-segment fault geometry, **b** using one-segment fault geometry

Table 4 Inversion results by using uniform and non-uniform FEM with three- and one-segment fault

	RMSE descending dataset (m)	RMSE ascending dataset (m)	Maximum slip (m)	Smoothing factor	RMSE (m)	Moment (Nm)	Magnitude
One segment uniform	0.0427	0.0476	4.45	0.15	0.0452	2.41×10^{19}	6.9215
One segment non-uniform	0.0435	0.0462	4.48	0.15	0.0448	2.47×10^{19}	6.9289
Three segments uniform	0.0435	0.0403	4.5163	0.1	0.042	2.30×10^{19}	6.9079
Three segments non-uniform	0.0441	0.0396	4.47	0.1	0.042	2.35×10^{19}	6.9146

In homogeneous half-spaces, surface deformation is determined by the seismic moment and a factor containing the relative elastic parameters ($\alpha = (\lambda + \mu) / (\lambda + 2\mu)$; λ and μ are Lamé parameters) (Okada 1992). In layered half-space, the factor α is not applicable because the situation is more complicated, where the surface deformation depends on the contrast of the elastic moduli (here they are Young modulus and Poisson's ratio) in different layers. Such physical discrepancy between layered and homogeneous half-space leads to the different moments derived from non-uniform FEM and uniform FEM. However, as mentioned earlier, the moment difference between layered and homogeneous FEM is not very obvious. The reason is possibly that the uppermost layer in non-uniform FEM is larger than 30 km over most of the area, and then the seismogenic zone would be fully embedded in the upper elastic layer. Thus, surface deformation is mostly influenced by the uppermost layer, and therefore the layered effect has very little influence in derived moment of non-uniform FEM.

4.4 Comparison with other results

The source characteristics of the YE have also been explored by analytical methods in some recent published researches (Elliott et al. 2010; Shan et al. 2010).

Both of their results suggest that the location of the largest slip is similar to our results.

Shan's result suggests three slip concentrations on the Yutian fault plane; however, this study only finds two and the resultant peak slip value is lower. Comparing the inversion data and parameter settings between these two studies, there are mainly three changes in this work that may account for these differences: (1) additional ascending Envisat data are included, (2) smoothing factor is increased, and (3) fault geometry changes from arc-shaped to three-segment. In the absence of these analysis differences, the derived slip distribution is almost the same as Shan's result (Fig. 9a). Our results show that the central concentration has disappeared if the ascending Envisat data are included and the maximum slip value has dropped to ~4 m when the smoothing factor was increased. The above strike test (Fig. 4) shows that the third change would further divide the single slip concentration in arc-shaped geometry into two slip concentrations separately located in different segments.

Elliott's result suggests a much deeper distribution which does exist in this study, and it gives a moment magnitude of 7.1, a little higher than our result. Since we have used similar fault geometry, a possible reason for the difference is the geodetic data. Elliott's study included an extra ALOS ascending pass data, and the Envisat image pairs they used have better coherence near the fault; therefore, the deeper slip is likely to be derived from

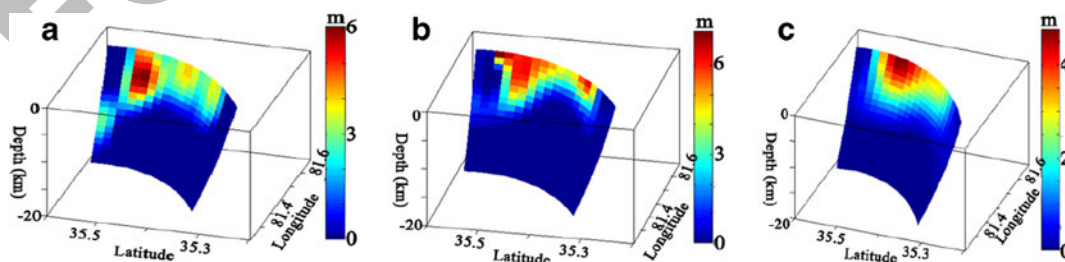


Fig. 9 Slip results comparing with Shan's study by taking several parameters settings. **a** Without changes from Shan's study, **b** including ascending Envisat data, **c** taking larger smoothing factor

the additional constraints. This additional slip could consequently increase the derived moment magnitude.

5 Conclusions

Using InSAR observation of YE, we conducted a series of inversions with various parameter settings and different models. The major conclusions can be summarized as follows:

1. The three-segment geometry can best describe the fault of YE, and the dip angle and strike determined from Harvard CMT and Quickbird image are acceptable because the corresponding residual is close to the lowest RMSE. The difference between uniform FEM and Okada is larger than the difference between non-uniform and uniform FEM. It means that the improvement brought by considering geologic satisfying situation in FEM is less than the uncertainties caused by numerical artifacts presumably associated with an overly coarse FEM mesh, implying that the Okada model is more reliable than FEM in this case. Among all the results using different models and various parameter settings in this study, the most reliable inversion result to describe the YE comes from the three-segment Okada model with dip and strike parameters given by Harvard CMT and Quickbird image.

2. According to the inversion results from the three-segment Okada model, there are two slip concentrations respectively located on the central segment and the south segment of the fault plane. The central segment is almost pure normal faulting, while the south segment has a small left-lateral movement. The largest slip was found in the central segment breaking to the surface, with a value of 4.4 m. The estimated seismic moment is 2.34×10^{19} Nm, equal to an event of Mw 6.91.

3. FEMs provide a flexible approach for building a geologic satisfying model to solve for earthquake displacement. Some complex earth structures that are hard to simulate with analytical methods, such as lateral variation and multi-segment faults conjunction, can be addressed by using FEMs. The advantage of FEMs can be fully presented when modeling the earthquake occurring in areas with obvious lateral variations, where neither a homogeneous nor a layered half-space is a good approximation for the medium (e.g., the boundary between sea plate and continental plate) (Masterlark and Hughes 2008; Zhao et al. 2004). However, FEMs contain

inevitable errors associated with the numerical approximation (e.g., linear basis functions) of partial differential equations. In order to reduce the influence of these errors, FEMs may require a larger smoothing factor compared to that for an Okada model. Considering the high computational cost of FEMs, an Okada model is an acceptable choice when the geologic situation is not too complex to be simulated with HEHS assumptions.

Acknowledgments This work was supported by the National Science Foundation (40874006), Basic Scientific Funding of Institute of Geology, China Earthquake Administration (LED2008A06), and Projects in the National Science & Technology Pillar Program (2008BAC35B04). Support for TM is provided, in part, by the US NSF EAR-0911466. We also thank Dr. Wang Rongjiang for providing SDM code and Prof. Zhang Jingfa for providing the ascending-pass ENVISAT/ASAR data. Academic licensing for Abaqus software is provided by Simulia, Dassault Systèmes.

References

- China Seismological Bureau (1992) The Altun active fault zone. China Seismological Press, Beijing, pp 1–319
- Chlie M, Avouac JP, Hjorleifsdottir V, Song TRA, Ji C, Sieh K, Sladen A, Hebert H, Prawirodirdjo L, Bock Y (2007) Coseismic slip and afterslip of the great Mw 9.15 Sumatra–Andaman earthquake of 2004. *Bulletin of the Seismological Society of America* 97:S152
- Christensen N (1996) Poisson's ratio and crustal seismology. *J Geophys Res* 101:3139–3156
- Currenti G, Del Negro C, Scandura D, Williams CA (2008) Automated procedure for InSAR data inversion using finite element method. In: Use of remote sensing techniques for monitoring volcanoes and seismogenic areas. USEReST 2008. Second Workshop, 1–5. Nov. 2008
- Elliott J, Walters R, England P, Jackson J, Li Z, Parsons B (2010) Extension on the Tibetan plateau: recent normal faulting measured by InSAR and body wave seismology. *Geophys J Int* 183:503–535
- Fialko Y (2006) Interseismic strain accumulation and the earthquake potential on the southern San Andreas fault system. *Nature* 441:968–971
- Grilli ST, Harris JC, Tajalibakhsh T, Masterlark TL, Kyriakopoulos C, Kirby JT, Shi F (2012) Numerical simulation of the 2011 Tohoku tsunami based on a new transient FEM co-seismic source. *Pure and Applied Geophysics*, in press
- Guerrieri L, Baer G, Hamiel Y, Amit R, Blumetti A, Comerci V, Di Manna P, Michetti A, Salamon A, Mushkin A (2010) InSAR data as a field guide for mapping minor earthquake surface ruptures: ground displacements along the Paganica Fault during the 6 April 2009 L'Aquila earthquake. *J Geophys Res* 115:B12331
- Hayes G, Briggs R, Sladen A, Fielding E, Prentice C, Hudnut K, Mann P, Taylor F, Crone A, Gold R (2010) Complex rupture during the 12 January 2010 Haiti earthquake. *Nat Geosci* 3:800–805

- Hearn EH, Burgmann R (2005) The effect of elastic layering on inversions of GPS data for coseismic slip and resulting stress changes: strike-slip earthquakes. *Bull Seismol Soc Am* 95:1637–1653
- Hu Y, Wang K, He J, Klotz J, Khazaradze G (2004) Three-dimensional viscoelastic finite element model for postseismic deformation of the great 1960 Chile earthquake. *J Geophys Res* 109:B12403
- Jonsson S, Zebker H, Segall P, Amelung F (2002) Fault slip distribution of the 1999 Mw 7.1 Hector Mine, California, earthquake, estimated from satellite radar and GPS measurements. *Bull Seismol Soc Am* 92:1377–1389
- Masterlark T (2003) Finite element model predictions of static deformation from dislocation sources in a subduction zone: sensitivities to homogeneous, isotropic, Poisson-solid, and half-space assumptions. *J Geophys Res* 108(B11):2540
- Masterlark T, Hughes K (2008) Next generation of deformation models for the 2004 M9 Sumatra–Andaman earthquake. *Geophys Res Lett* 35:L19310
- Masterlark T, Lu Z (2004) Transient volcano deformation sources imaged with interferometric synthetic aperture radar: application to Seguam Island, Alaska. *J Geophys Res* 109: B01401
- Masterlark T, DeMets C, Wang H, Sanchez O, Stock J (2001) Homogeneous vs heterogeneous subduction zone models: coseismic and postseismic deformation. *Geophys Res Lett* 28:4047–4050
- Melosh H, Raefsky A (1981) A simple and efficient method for introducing faults into finite element computations. *Bull Seismol Soc Am* 71:1391–1400
- Molnar P, Burchfiel B, K'uangyi L, Ziyun Z (1987) Geomorphic evidence for active faulting in the Altyn Tagh and northern Tibet and qualitative estimates of its contribution to the convergence of India and Eurasia. *Geology* 15:249
- Okada Y (1985) Surface deformation due to shear and tensile faults in a half-space. *Bull Seismol Soc Am* 75:1135–1154
- Okada Y (1992) Internal deformation due to shear and tensile faults in a half-space. *Bull Seismol Soc Am* 82:1018–1040
- Pollitz FF (1996) Coseismic deformation from earthquake faulting on a layered spherical earth. *Geophys J Int* 125:1–14
- Qiusheng L, Rui G, Deyuan L, Jingwei L, Jingyi F, Zhiying Z, Wen L, Yingkang L, Quanren Y, Dexing L (2002) Tarim underthrust beneath western Kunlun: evidence from wide-angle seismic sounding. *J Asian Earth Sci* 20:247–253
- Rybicki K (1971) The elastic residual field of a very long strike-slip fault in the presence of a discontinuity. *Bull Seismol Soc Am* 61:79–92
- Savage J (1987) Effect of crustal layering upon dislocation modeling. *J Geophys Res* 92:10595–10600
- Savage J (1998) Displacement field for an edge dislocation in a layered half-space. *J Geophys Res* 103:2439–2446
- Schmidt D, Burgmann R (2006) InSAR constraints on the source parameters of the 2001 Bhuj earthquake. *Geophys Res Lett* 33:L02315
- Shan X, Zhang G, Wang C, Qu C, Song X, Guo L (2010) Source characteristics of the Yutian earthquake in 2008 from inversion of the co-seismic deformation field mapped by InSAR. *J Asian Earth Sci* 40:935–942
- Shao XZ, Xu SB (1997) Crust structural characteristics of Tarim basin. *Pet Explor Dev* 24:1–5
- Shen F, Royden L, Burchfiel B (2001) Large-scale crustal deformation of the Tibetan plateau. *J Geophys Res* 106:6793–6816
- Shen ZK, Sun J, Zhang P, Wan Y, Wang M, Burgmann R, Zeng Y, Gan W, Liao H, Wang Q (2009) Slip maxima at fault junctions and rupturing of barriers during the 2008 Wenchuan earthquake. *Nat Geosci* 2:718–724
- Smith AT (1974) Time-dependent strain accumulation and release at island arcs: implications for the 1946 Nankido earthquake. Dissertation, Massachusetts Institute of Technology, Cambridge, p 292
- Sun J, Shi Y, Shen Z, Xu X, Liang F (2007) Parameter inversion of the 1997 Mani earthquake from InSAR co-seismic deformation field based on linear elastic dislocation model. *Chin J Geophys* 50:1390–1397
- Trasatti E, Kyriakopoulos C, Chini M (2011) Finite element inversion of DInSAR data from the Mw 6.3 L'Aquila earthquake, 2009 (Italy). *Geophys Res Lett* 38:L08306
- Wallace K, Yin G, Bilham R (2004) Inescapable slow slip on the Altyn Tagh fault. *Geophys Res Lett* 31:L09613
- Wang H (2000) Theory of linear poroelasticity: with applications to geomechanics and hydrogeology. Princeton University Press, Princeton, p 287
- Wang C, Shan X, Zhang G, Guo L, Han Y (2009) Finite element method to invert coseismic slip of Yutian earthquake from InSAR. In Proc SPIE 7841:78410L
- Wang C, Ding X, Shan X, Zhang L, Jiang M (2012) Slip distribution of the 2011 Tohoku earthquake derived from joint inversion of GPS, InSAR and seafloor GPS/acoustic measurements. *Journal of Asian Earth Sciences*. doi:10.1016/j.jseaes.2012.06.019
- Wegmuller U, Werner C (1997) Gamma SAR processor and interferometry software. ESA SP-414:1687–1692
- Wright TJ, Lu Z, Wicks C (2003) Source model for the Mw 6.7, 23 October 2002, Nenana Mountain earthquake (Alaska) from InSAR. *Geophys Res Lett* 30:1974
- Wright TJ, Lu Z, Wicks C (2004) Constraining the slip distribution and fault geometry of the Mw 7.9, 3 November 2002, Denali fault earthquake with interferometric synthetic aperture radar and global positioning system data. *Bull Seismol Soc Am* 94:S175
- Zhang P, Molnar P, Xu X (2007) Late Quaternary and present-day rates of slip along the Altyn Tagh Fault, northern margin of the Tibetan plateau. *Tectonics* 26:TC5010
- Zhang G, Qu C, Shan X, Song X, Wang C, Hu JC, Wang R (2011) Slip distribution of the 2008 Wenchuan Ms 7.9 earthquake by joint inversion from GPS and InSAR measurements: a resolution test study. *Geophys J Int* 186:207–220
- Zhao S, Muller R, Takahashi Y, Kaneda Y (2004) 3-D finite-element modelling of deformation and stress associated with faulting: effect of inhomogeneous crustal structures. *Geophys J Int* 157:629–644